Device

Article

Nonvolatile electrochemical memory at 600°C enabled by composition phase separation

Graphical abstract

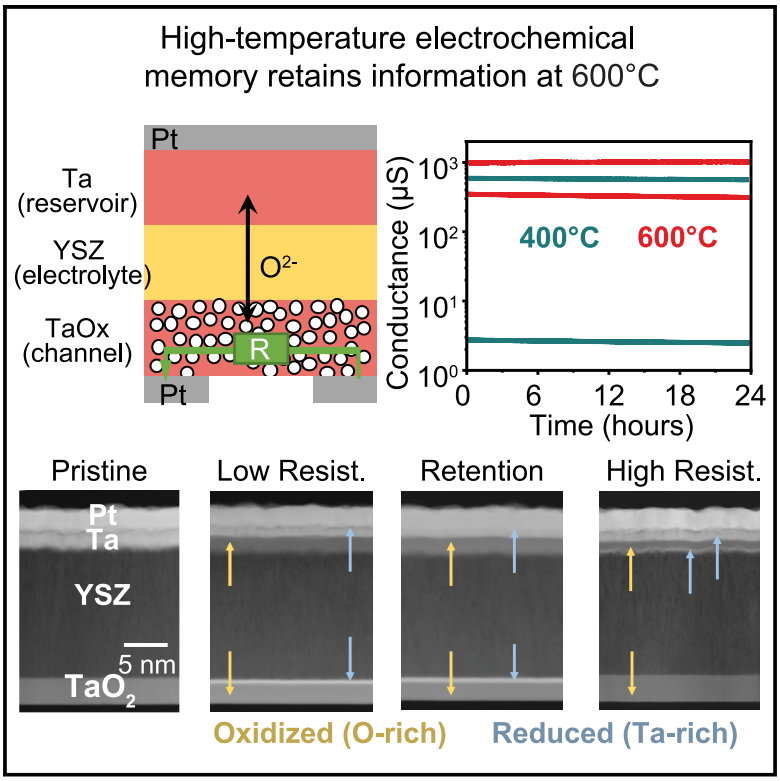

Highlights

- A solid-state memory device can switch and retain information at 600°C
- Information is stored via the electrochemical migration of oxygen vacancies
- Composition phase separation enables long-term information storage
- Transmission electron microscopy directly visualizes phase separation

Authors

Jingxian Li, Andrew J. Jalbert, Sangyong Lee, ..., Elliot J. Fuller, A. Alec Talin, Yiyang Li

Correspondence

jxli@umich.edu (J.L.), yiyangli@umich.edu (Y.L.)

In brief

Silicon-based microelectronic devices have traditionally been limited to temperatures below <150°C. In this work, we develop a solid-state memory cell that can retain information at temperatures as high as 600°C. This device stores information by electrochemically shuttling oxygen ions between two tantalum oxide electrodes in a process that resembles that of a Li-ion battery. Long-term information retention is attained through composition-driven phase separation of the tantalum oxide electrode.

Explore
Early prototypes with exciting performance and new methodology

Li et al., 2025, Device 3, 100623
April 18, 2025
https://doi.org/10.1016/j.device.2024.100623

CellPress

Please cite this article in press as: Li et al., Nonvolatile electrochemical memory at 600°C enabled by composition phase separation, Device (2024), https://doi.org/10.1016/j.device.2024.100623

Device

CellPress
OPEN ACCESS

Article

Nonvolatile electrochemical memory at 600°C enabled by composition phase separation

Jingxian Li,[1,*] Andrew J. Jalbert,[1] Sangyong Lee,[1] Leah S. Simakas,[1] Noah J. Geisler,[1] Virgil J. Watkins,[1] Laszlo A. Cline,[1] Elliot J. Fuller,[2] A. Alec Talin,[2] and Yiyang Li[1,3,*]

[1]Materials Science and Engineering, University of Michigan, Ann Arbor, MI 48109, USA
[2]Sandia National Laboratories, Livermore, CA 94550, USA
[3]Lead contact
*Correspondence: jxli@umich.edu (J.L.), yiyangli@umich.edu (Y.L.)
https://doi.org/10.1016/j.device.2024.100623

THE BIGGER PICTURE Moore's law has led to monumental advances in computing over the past 50 years. However, one shortcoming of silicon-based logic and memory devices is their limited temperature range, typically <150°C. In this work, we present a solid-state memory device that can operate and store information at temperatures as high as 600°C. Rather than relying on the motion of electrons, this device stores information through the electrochemical migration of oxygen ions in transition metal oxides, a process that resembles that of solid oxide fuel cells and batteries. This memory device can expand the use of microelectronics in extreme environments, like deep energy wells, turbine engines, and space.

SUMMARY

Silicon-based microelectronics are limited to ~150°C and therefore not suitable for the extremely high temperatures in aerospace, energy, and space applications. While wide-band-gap semiconductors can provide high-temperature logic, nonvolatile memory devices at high temperatures have been challenging. In this work, we develop a nonvolatile electrochemical memory cell that stores and retains analog and digital information at temperatures as high as 600°C. Through correlative scanning transmission electron microscopy, we show that this high-temperature information retention is a result of composition phase separation between the oxidized and reduced forms of amorphous tantalum oxide. This result demonstrates a memory concept that is resilient at extreme temperatures and reveals phase separation as the principal mechanism that enables nonvolatile information storage in these electrochemical memory cells.

INTRODUCTION

Conventional Si-based digital electronics are typically limited to 150°C due to the rise in the intrinsic carrier concentration with temperature.[1] This limitation precludes high-temperature applications,[2] including in aerospace and automotive engines (150°C–600°C), interplanetary exploration such as Venus (550°C), and the extraction of petroleum and geothermal energy from deep wells (300°C–600°C).[1] Logic and memory form the foundation for modern computing. While high-temperature logic can be developed using wide-band-gap semiconductors like silicon carbide (SiC)[3,4] and gallium nitride (GaN),[5] as well as emerging technologies like carbon nanotubes,[6] the development of memory units for such extreme temperatures has been more challenging. Presently, the only re-writeable memories[7,8] that have retained nonvolatile information above 500°C are nanogap resistive memory[9] and nitride-based ferroelectric memory[10,11]; these emerging technologies exhibit limitations such as large cycle-to-cycle variations, destructive read, and/or high switching voltages.

Electrochemical random-access memory (ECRAM) has recently emerged as a promising solution for analog computing.[12–16] ECRAM is a three-terminal memory device that stores and switches information through ion migration and the resulting change in valence and electronic conductivity. ECRAM research is primarily focused on three types of ions: Li^+,[17–21] H^+,[22–26] and O^{2-}[27–37]; other ions, like Cu^{+}[38] and Mg^{2+},[39] have also been studied. Oxygen-based ECRAM operates by electrochemically transporting oxygen ions (or vacancies) between two mixed ionic and electronic conducting (MIEC) metal oxides with a solid electrolyte. This mechanism allows ECRAM to switch resistance states by modulating the oxygen concentration in the MIEC metal oxides. Early demonstrations of oxygen ion ECRAM based on titanium[28] or tungsten[27] oxides achieved a high density of analog states but

Please cite this article in press as: Li et al., Nonvolatile electrochemical memory at 600°C enabled by composition phase separation, Device (2024), https://doi.org/10.1016/j.device.2024.100623

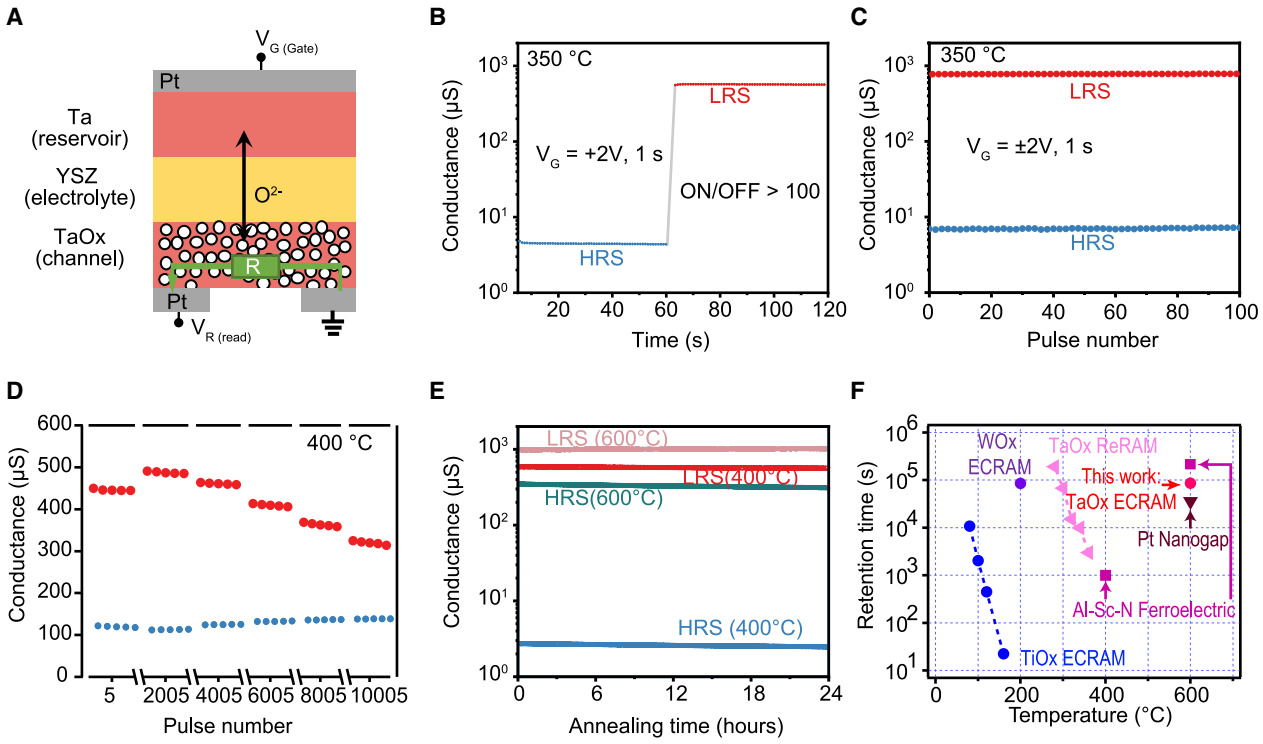

Figure 1. Binary switching and high-temperature retention of TaOx ECRAM devices

(A) Schematic depicting the structure of the ECRAM device, featuring a stacked configuration of TaO_X/YSZ/Ta. This design utilizes an electric field to facilitate the movement of oxygen ions through the YSZ electrolyte, effectively modulating the oxygen concentration in the TaO_X channel oxide to enable the storage of information through the creation of varying resistance states in the device.

(B) Binary switching behavior from HRS to LRS with one pulse (2 V, 1 s) at 350°C shows an on/off ratio of more than 100.

(C) 50-cycle switching between LRS and HRS with minimal cycle-to-cycle variation.

(D) Write endurance measurements at 400°C show operations for greater than 10,000 write pulses; the read endurance is given in Figure S2.

(E) The retention measurements of two resistance states at 400°C and 600°C for 24 h. At 400°C, the LRS conductance decreased by 5%, and the HRS conductance decreased by 10% after 24 h; at 600°C, the LRS conductance increased by 5%, while the HRS conductance decreased by 12% after 24 h.

(F) Retention times of various memory devices, including our ECRAM with TaO_X, Pt nanogap devices,[9] $Al_{0.7}Sc_{0.3}N$ ferroelectrics,[10,11] ReRAMs based on TaO_X,[43] and ECRAMs utilizing TiO_X[28] and WO_X.[40]

suffered from poor state retention times (<1 day at room temperature). Recently, it was shown that tungsten oxide-based ECRAM can yield ~24 h of retention at 200°C under short circuit,[40] which projects to over 10 years at 85°C. However, this device was constructed on single-crystal yttria-stabilized zirconia (YSZ) crystal substrate and, therefore, not CMOS compatible. Moreover, there is no clear pathway for operation above 200°C.

In this work, we developed a high-temperature-stable ECRAM device utilizing amorphous TaO_x deposited on a Si/SiO_2 substrate that is capable of recording and retaining binary and multi-level analog conductance states at temperatures up to 600°C. Importantly, we obtain over 24 h of retention at short circuit at 600°C, a notable advancement in the resilience of electrochemical memory devices. We propose that these findings are a result of amorphous phase separation between the Ta and $TaO_{1.9}$,[41,42] which have been shown to facilitate information retention in TaO_x-based resistive memory devices.[42] Our correlative transmission electron microscopy shows clear evidence of this phase separation. Our results demonstrate a promising path toward the realization of high-temperature analog and binary resistive memory.

RESULTS

TaOx-based ECRAM as high-temperature nonvolatile binary memory

The structure of our TaO_X-ECRAM cells consists of a 20 nm reservoir layer of tantalum, a 140 nm electrolyte layer of YSZ electrolyte, and a 20 nm channel layer of amorphous oxygen-deficient tantalum suboxide (TaO_X) deposited on SiO_2 (500 nm)/Si substrates using sputtering (Figures 1A and S1). Three Pt current collectors are sputtered using shadow masks to serve as the gate, source, and drain electrodes. Finally, a passivation layer of SiN_X is deposited to protect the tantalum oxide from moisture and oxygen in the environment.

We switch this device by applying either a positive or a negative gate voltage (V_G), typically +2 V to increase (SET) or −2V to decrease (RESET) the channel conductance. This applied electrochemical voltage moves oxygen ions between the gate and the channel, which changes the channel conductance. The channel conductance depends on the coulombs of ions transferred, which is given by the time integral of the current; this makes the channel conductance strongly hysteretic and

Please cite this article in press as: Li et al., Nonvolatile electrochemical memory at 600°C enabled by composition phase separation, Device (2024), https://doi.org/10.1016/j.device.2024.100623

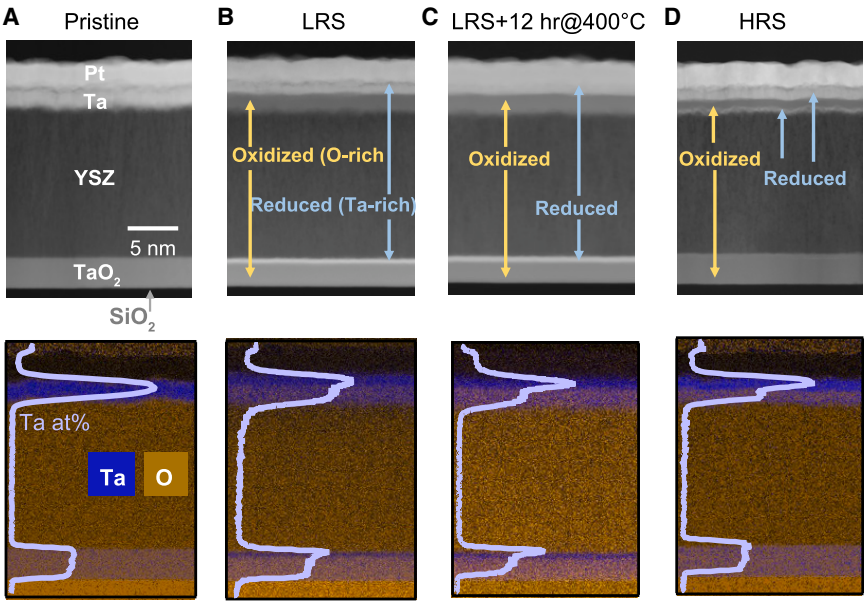

Figure 2. STEM of cross-sectioned ECRAM devices

The top row shows the high-angle annular dark field (HAADF) mapping, while the bottom row shows energy-dispersive spectroscopy (EDS) mapping. The Ta atom % is plotted as a function of the depth.

(A) Pristine devices fabricated using a Ta ion reservoir and a TaO_2 channel; this sample was not annealed at 400°C after fabrication.

(B) In the low-resistance state (LRS), the ion reservoir is partially oxidized, while a reduced Ta-rich, O-poor layer is formed at the channel.

(C) The LRS device maintains its metal and oxygen distribution even after short-circuiting the device for 12 h at 400°C. This coexistence of oxidized and reduced TaO_X compounds over time in both the reservoir and the channel is consistent with the composition phase separation of the material and the nonvolatile information retention of the device.

(D) The HRS state shows that the channel is again oxidized, while a reduced Ta-rich layer forms at the reservoir layer.

therefore dependent on the voltage applied over time. As a result, ECRAM's switching mechanism is different from that of a three-terminal field-effect transistor. During retention measurements, we ground the gate by applying 0 V, short-circuiting it to the channel. No switch or selector was used in these experiments. All fabrication was conducted at room temperature with a 1 h annealing at 400°C to improve the crystallinity of the YSZ but still maintain thermal compatibility with back-end-of-line processes. More details can be found in the experimental procedures.

We initially assess the binary switching behavior. Figure 1B illustrates the SET process, showcasing a >100 on/off ratio differentiating between the high-resistance state (HRS) and low-resistance state (LRS) with ±2 V for 1 s at 350°C. This SET/RESET switching is reproducible with minimal cycle-to-cycle variation (Figure 1C). Moreover, the write endurance exceeds 10,000 pulses at 400°C (Figure 1D). The read speed is as short as 1 μs, while the read endurance exceeds 10^6 pulses (Figure S2). Figure S3 shows that resistance switching could be obtained effectively across a broad temperature range of 200°C–600°C, rendering this technology adaptable for diverse high-temperature applications. To assess the temperature-dependent switching, we further conducted a comprehensive examination of temperature's influence on switching behavior by utilizing a consistent 2-V, 1-s pulse across a temperature span from 300°C to 550°C (Figure S4). Our findings reveal that the highest on/off ratios (>100) are obtained for temperatures ranging between 350°C and 400°C (Figure S5). However, at temperatures below 300°C, the sluggish oxygen diffusivity in our metal oxides impedes sufficient ion migration for higher on/off ratios. At temperatures above 450°C, the HRS conductance increases due to an increase in the electronic conductivity of TaO_2 with temperature and, thus, reduces the on/off ratio. The overall switching speed is fairly slow due to the high Arrhenius activation energy of oxygen (>1 eV); however, as seen in Figure S3, the speed increases at higher temperatures due to the increased oxygen mobility with higher thermal energies.[28]

We tested the retention of the device under short circuit at temperatures between 400°C and 600°C. These results show less than a 12% change in the conductance after 24 h over these temperatures (Figures 1E and S6). Figure 1F shows a comparative analysis of the retention times between our TaO_x-ECRAM and other high-temperature memory technologies (Figure 1F). At 600°C, our ECRAM cell has a temperature performance similar to Pt-nanogap Resistive Random-Access Memory (ReRAM)[9] and $Al_{0.7}Sc_{0.3}N$ ferroelectric capacitors[10]; a comparative analysis of these devices will be given under discussion. ECRAMs utilizing TiO_x[28] and WO_x[40] show substantially reduced retention compared to the TaO_X ECRAM device shown here. Likewise, filament-based ReRAM devices using similar materials[44] yield substantially lower retention compared to the TaO_X ECRAM cell (Figure 1F). We note that these measurements were conducted in an inert Ar environment with ~3 ppm O_2; in an oxidizing environment, the ~60 nm SiN_X barrier layer is not sufficient to prevent the TaOx layers from oxidation (Figure S7). Additional oxygen diffusion barriers would be necessary for high-temperature operation in more oxidizing environments.

Direct visualization of phase separation in TaO_X ECRAM

To shed light on the mechanism of the above resistive switching and retention behaviors in TaO_X-based ECRAM, we performed scanning transmission electron microscopy (STEM) on cross-sectioned devices. Figure 2A depicts high-angle annular dark field (HAADF) and energy-dispersive spectroscopy (EDS) mapping of Ta L-edge and O K-edge from a pristine Ta/YSZ/TaO_2 device. Although the EDS atomic ratios are not fully quantitative, they are consistent with a metallic Ta ion reservoir and a TaO_2 channel based on our deposition recipes. Next, we consider a device after switching to the LRS (Figure 2B). On the channel side, we observe an ~5 nm reduced Ta-rich layer

Please cite this article in press as: Li et al., Nonvolatile electrochemical memory at 600°C enabled by composition phase separation, Device (2024), https://doi.org/10.1016/j.device.2024.100623

at the electrolyte/channel interface and a corresponding ~15 nm oxidized TaO_X at the reservoir/electrolyte interface. These results are consistent with the migration of oxygen ions from the channel layer through the electrolyte in response to the applied electric field, ultimately reaching the Ta reservoir. The reduced Ta-rich layer at the channel is also consistent with the increased conductance of the LRS. Furthermore, electrical measurements of the LRS channel resistance as a function of the temperature (Figure S8) show very little temperature dependence, again consistent with a metallic Ta-rich region observed under STEM (Figure 2B). In contrast, the HRS shows substantial temperature dependence, which suggests an oxidized channel consisting of a metal oxide semiconductor or insulator (Figures 2A and 2D).

The increased thickness of the reservoir may be attributed to volumetric expansion due to the oxidation of the Ta to TaO_X, while the reduced channel undergoes slight contraction due to the loss of oxygen ions. Our STEM results provide direct microscopy evidence to show the electrochemical migration of oxygen in ECRAM devices.

We next investigate retention by imaging a different LRS device after 12 h of short circuit at 400°C (Figure 2C). The tantalum and oxygen distribution remains essentially unchanged compared to that observed in the LRS device without this high-temperature annealing (Figure 2B). This observation is consistent with the stability of the electrical resistance over this time (Figure 1D). We attribute this stability to the phase separation of the tantalum and oxygen within the device, which appears to play a crucial role in retaining the chemical state and, by extension, the electrical properties under thermal stress (Figure 1E). Specifically, within the miscibility gap, the oxygen chemical potential of all compositions of Ta and O is equal (Figure S9), which is discussed in detail our previous work.[42] For this reason, the coexistence of oxidized and reduced layers in both the channel and the reservoir is a stable configuration; it will not revert to a single homogeneous film over time. For the same reason, the oxygen chemical potentials in the reservoir and channel are equal regardless of the thickness of the reduced Ta-rich layer in the channel. As a result, oxygen has no preference to migrate from the gate to the channel or vice versa, resulting in the retention stability of the device in Figure 1D. In other words, the long retention of our ECRAM device at high temperature under short circuit is enabled by the absence of any chemical driving forces to move the oxygen ions between the reservoir and channel.

In Figure 2D, we image the HRS after resetting the device. The channel composition resembles the pristine device shown in Figure 2A but with a slight increase in the Ta concentration. This likely accounts for the higher conductance seen in the HRS (~3 μS at 400°C) relative to the pristine configuration (<0.1 μS). Conversely, the HRS shows a reduced Ta layer at the reservoir-electrolyte interface and an oxidized layer above it, distinguishing it from both the pristine and the LRS state. We hypothesize that there is a net transfer of oxygen from the YSZ electrolyte to the metallic Ta reservoir during the initial heating process, thereby making the reservoir in the HRS more oxidized than in the pristine device. However, this oxidation process is expected to be self-limiting because there is a finite amount of excess oxygen in the YSZ electrolyte. Figure S10 shows that the Ta metal conductance increases when annealed at 500°C for 100 h. This suggests that the Ta film remains metallic over this time frame and that the increase in the conductance is likely a result of increased crystallinity upon annealing.

To further illustrate the role of phase separation, we conduct cyclic voltammetry between the reservoir/gate and the channel (Figure 3A). The results show clear oxidation and reduction peaks corresponding to the SET and RESET of the device. When a positive voltage is applied to the gate, the positive gate current indicates that negatively charged oxygen ions are moved from the channel to the ion reservoir. This results in the formation of a reduced Ta-rich layer in the channel, increasing the channel conductance (Figure 3C). However, upon further increase of the voltage, the gate current decreases substantially, which most likely suggests a depletion of oxygen from the channel. A similar behavior is observed upon reversing the voltage, whereby a negative current implies that oxygen moves from the gate to the channel (Figure 3A), reducing the channel conductance (Figure 3B). This result is largely repeatable from one cycle to the next.

The total integrated charge is about 170 micro-coulombs in each direction, or 5.3×10^{14} oxygen ions. With an estimated channel volume of 1.7×10^{13} nm^3 (500 μm × 1750 μm × 20 nm), our results suggest that 30 oxygen ions are transferred for every cubic nanometer of device volume. Crystalline Ta_2O_5 has about 50 oxygen ions per cubic nanometer based on a density of 7.8 g cm^{-3} and a molar mass of 442 g mol^{-1}. Assuming that the amorphous TaO_2 channel has a similar volume density of oxygen as bulk crystalline Ta_2O_5, then the total charge transferred in the cyclic voltammetry suggests that most of the available oxygen has been transferred between the channel and ion reservoir. In contrast, our STEM images only show a partial reduction of the channel (Figure 2B) because the switching was only conducted for 1 s.

The cyclic voltammetry sweeps also help us understand retention mechanisms, which show clear hysteretic behavior (Figure 3D). According to Figure 3B, there is no electrochemical gate current at 0 V regardless of whether the channel was previously reduced (SET) or oxidized (RESET). This result indicates that there is no migration of oxygen between the gate and the channel at 0 V and is consistent with the nonvolatility observed at high temperatures (Figure 1). This result is again consistent with phase separation, whereby the chemical potentials of the channel and reservoir are equal, thereby resulting in no electrochemical current when the voltage equals 0. In contrast, previous cyclic voltammetry on a TiO_2 ECRAM device shows a more capacitive profile, where there exists a substantial current at 0 V (Figure 3C). This nonzero current reverses the oxygen migration forced at positive and negative voltages, resulting in a loss of information over time.

Analog multilevel switching

In addition to binary switching, our TaO_X-ECRAM cells exhibit analog switching characteristics, which align with the traits observed in previous room-temperature ECRAM cells.[12] This device attains and sustains 100 analog states through sub-millisecond pulses at 400°C, as illustrated in Figure 4A. These properties mirror those found in other ECRAMs and highlight the device's

Please cite this article in press as: Li et al., Nonvolatile electrochemical memory at 600°C enabled by composition phase separation, Device (2024), https://doi.org/10.1016/j.device.2024.100623

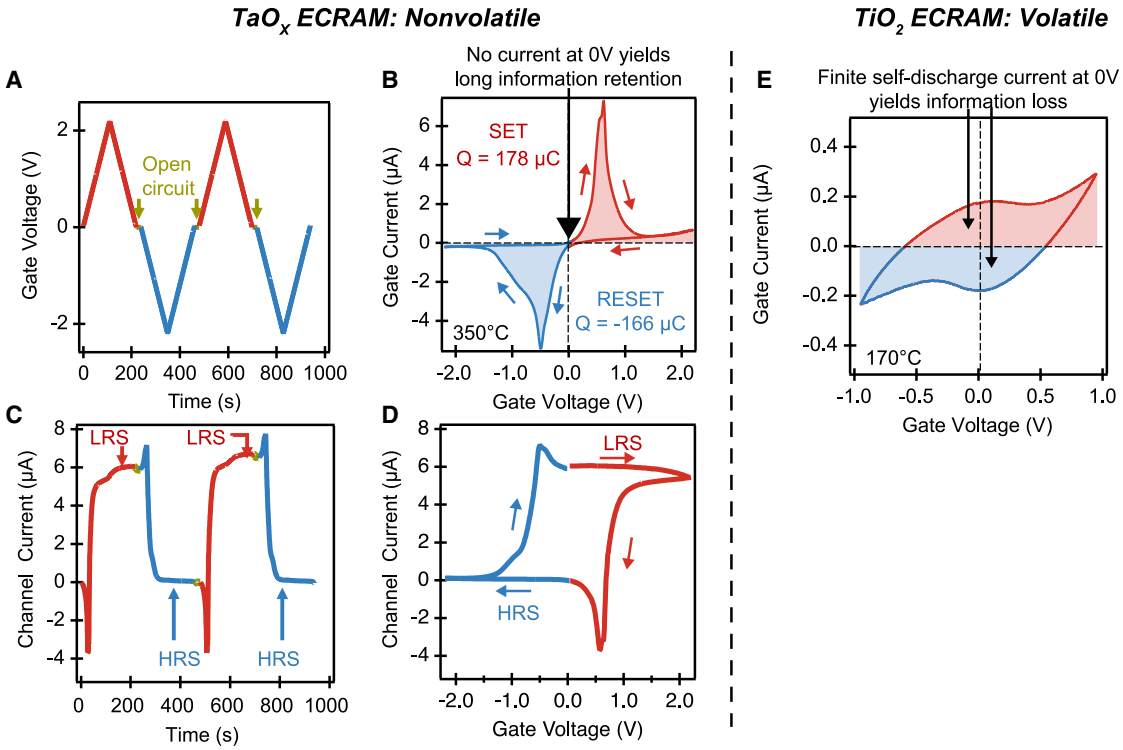

Figure 3. Cyclic voltammetry analysis of the ECRAM device

(A) Cyclic voltammetry was conducted by cycling the voltage at a rate of 20 mV s^{-1} while maintaining a constant read voltage of 0.01 V across the channel.

(B) The gate current during the cyclic voltammetry shows clear redox peaks during SET and RESET. There is no electrochemical current at 0 V, consistent with the absence of an oxygen chemical potential difference between the reservoir and the channel.

(C) The channel current as measured with a 10-mV potential taken concurrently with the gate cyclic voltammetry. During switching (SET or RESET), the channel current is affected by the electrochemical gate current from (A).

(D) A plot of the channel current against the V_G shows a clear hysteresis between the HRS and the LRS after switching, consistent with its role as a nonvolatile memory.

(E) Cyclic voltammetry data for a volatile TiO_2-based ECRAM device from previous work[28] show a substantial negative current at 0 V after SET, resulting in information loss through an electrochemical self-discharge process. This contrasts with the TaOx ECRAM in (B).

ability for analog matrix multiplications for in-memory computing. Moreover, our devices show reproducible switching consistent with previous oxygen-based ECRAM cells.[27–29,45] Figures 4B and S11 show that the ECRAM device manifests analog behavior across different resistance values spanning from the micro-siemens to milli-siemens range This reliability and consistency further substantiate the device's potential for dependable analog data manipulation in various computational tasks.

In probing the analog switching behavior across pulse widths ranging from 500 µs to 4 ms at 8 V (Figure S12A), we observe linear dependence of analog switching with pulse width. A similar behavior has been observed with a negative pulse (Figure S12B). This indicates that the device's conductance can be finely tuned by altering the duration of the applied pulses. Similarly, Figure S13 shows that the conductance change is also linearly proportional to the pulse amplitude, consistent with previous reports in ECRAM.[28]

Finally, we conduct data retention tests for the analog states, summarized in Figure 4C. These tests show that the analog states ranging from 20 µS to over 800 µS maintained stable resistance after 12 h at 400°C. The observed phase separation within our device contributes to establishment of multiple equilibrium resistance states.

DISCUSSION

Our study presents a non-volatile ECRAM device concept based on amorphous, phase-separating TaO_X, demonstrating record ECRAM state retention in both binary and analog switching modes at temperatures as high as 600°C. The high-temperature performance is substantially better than that of commercial floating-gate memory (<150°C). It is also significantly better than that of all previously reported ECRAM types, which are limited to 200°C. Its temperature performance is comparable to that of recently demonstrated nitride-based ferroelectric memory[11] and Pt nanogap memory.[9] Compared to nitride ferroelectric memory, TaO_X ECRAM uses lower voltages (2 V vs. 15 V), can provide analog multi-level states, and has a higher on/off ratio (100 vs. 3 at 400°C, 3 vs. 1.5 at 600°C). Furthermore, its resistance information state can be "read" without disturbing the device. Compared to the nanogap memory, ECRAM has lower voltages (2 V vs. 6 V) and

Please cite this article in press as: Li et al., Nonvolatile electrochemical memory at 600°C enabled by composition phase separation, Device (2024), https://doi.org/10.1016/j.device.2024.100623

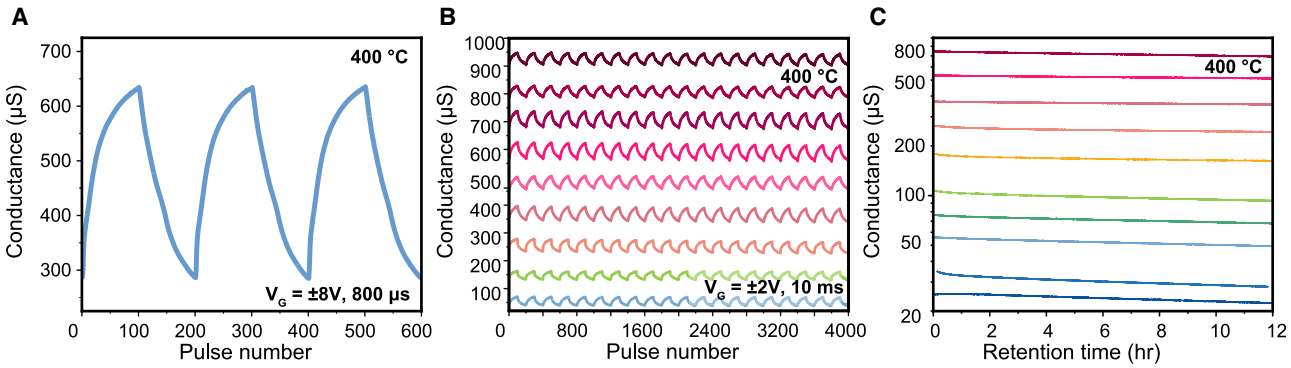

Figure 4. Analog switching and retention characterizations of the ECRAM

(A) Linear and symmetric conductance update in an ECRAM using a series of SET/RESET pulsing cycles of different pulse widths at 400°C (100 pulses, ±8 V, 800 µs).

(B) Small-amplitude analog switching around the many conductance states of the device. The switching alternates between 100 pulses of +2 V and 100 pulses of −2 V.

(C) Retention test of >10 analog states over a wide conductance window.

analog multi-level state capability (Figure 4), which can result in a higher density of information states. We note that these three emerging memory technologies utilize very different switching and information retention mechanisms; each device has its advantages and disadvantages, and are all viable candidates for high-temperature nonvolatile memory.

One weakness of our ECRAM cell is the high write temperature above 250°C. For low-temperature operations, we envision that it will be necessary to integrate a localized joule heater, as demonstrated recently for other oxygen-based ECRAM devices.[46,47] Additionally, while the on/off ratio is diminished at 600°C, this is a result of an increased conductance of the channel layer and could be mitigated by initially making the channel more oxidized. Further research is also needed to decrease the size of the device. Recent research has successfully shown micron- and nano-sized ECRAM devices based on proton[24,26] or oxygen ion[29] insertion into tungsten oxide using lithography processes. We anticipate that a similar process can be used to scale the tantalum oxide devices in this work.

Our STEM and electrochemistry results are consistent with an amorphous phase separation mechanism to explain the long-term retention in the TaO_x ECRAM. This design rule of using composition phase separation can also be used to engineer other types of ECRAMs, such as protonic ones, which have fast speed but limited retention under short circuit.[24,48] While our previous work also postulated that phase separation enables information retention in WO_X ECRAM,[40] this work showed direct evidence of phase separation using STEM (Figure 2) as well as operation at much higher temperature (600°C vs. 200°C). Moreover, the persistent coexistence of the Ta-rich and oxygen-rich regions provides additional evidence of phase separation in amorphous tantalum oxide within the device. This characterization result is consistent with our previous Auger depth profile measurements, which show that a Ta-rich and oxygen-rich bilayer film would not mix[42]; however, unlike in the previous work, the two layers in this work were created electrochemically *in situ* during device operation rather than deposited directly from vapor. This work also shows how phase separation can be harnessed in three-terminal ECRAM devices for high-temperature information storage just as they can be used to store information in two-terminal resistive memory based on tantalum oxide[42] and on lithium titanium oxide.[49,50]

Finally, we speculate regarding the possible ultimate switching temperature of this device. Tantalum oxide is also known to crystallize around 650°C[51]; this could represent the upper temperature limit. However, if we can make ECRAM using crystalline tantalum oxide, then it could point to much higher operational temperatures. According to the Ta-O phase diagram,[52] the miscibility gap extends to the melting temperature, which exceeds 1,500°C. In this regimen, the functionality of the other components, such as the SiN_X oxygen diffusion barrier, may limit the ultimate temperature limit.

CONCLUSION

We present a nonvolatile electrochemical memory that switches and retains information at 600°C for over 24 h. Our electrochemistry and TEM results suggest that phase separation occurs in the amorphous tantalum oxide channel and that this phase separation is responsible for the high-temperature stability of this device. This work shows new concepts that can be used to engineer nonvolatile memory for extreme environments.

EXPERIMENTAL PROCEDURES

Fabrication of TaO_X ECRAM cells

The ECRAM devices comprising thin-film YSZ were fabricated using an AJA Orion 8 Direct current (DC) / Radiofrequency (RF) sputter system (baseline pressure <5 e−7 torr) using shadow masks on a 1 cm die of Si with 500 nm of thermal oxide (University Wafers). The first shadow mask (Figure S1A) defines the bottom Pt electrode, which contains 5 nm of Ta adhesion layer and 20 nm of Pt. The Ta adhesion layer was DC sputtered at 100 W on a 3-in Ta target (99.95% purity; Plasmaterials) under pure Ar (6N purity). The Pt layer was DC sputtered at 100 W on a 2-in Pt target (99.99% purity, AJA) under pure Ar. The sputter gas pressure was 3 mtorr.

The second shadow mask (Figure S1B) defines the three successive oxide layers: the TaO_x channel, the YSZ electrolyte, and the Ta reservoir layer. The channel, or switching layer, consists of 20 nm of TaO_x and was DC sputtered at 100 W with the 3-in Ta target and a sputter gas mixture of Ar (6N):O_2 (5N) at a 37:3 ratio regulated by mass flow controllers. The sputter gas pressure was maintained at 5 mtorr with a substrate-to-target distance of approximately 15 cm. The 140 nm YSZ electrolyte was grown by RF sputtering on a 3-in YSZ target (8 mol % Y_2O_3 in ZrO_2, 99.9% purity, Plasmaterials) using a sputter power of 150 W and 5 mtorr of pure argon. The 20 nm Ta gate layer was grown by DC sputtering on a 3-in Ta target at a sputter power of 100 W in 5 mtorr of pure argon.

The third shadow mask (Figure S1C) was used to define the top gate contacts. It consists of 30-nm-thick gate Pt current collectors sputtered using the same process as the bottom contact, except without an adhesion layer. No additional annealing was performed during the room-temperature sputtering process. Finally, for environmental protection against oxidation, a 60 nm silicon nitride layer was deposited on the ECRAM device using plasma-enhanced chemical vapor deposition at 200°C in the Lurie Nanofabrication Facility via a Plasmatherm 790. The SiN_x above the current collectors was etched using reactive ion etching used a gaseous CF_4/O_2 mixture at a ratio of 95:5. The final devices are shown in Figures S1D and S1E. A 400°C anneal at 1 h was conducted in inert Ar to improve the crystallinity and ionic conduction of the YSZ electrolyte.

Device measurements

Following fabrication, the cell was tested in a six-probe Nextron MPS-Ceramic Heater CHH750 probe station. Three of the probes were used to contact the top gate electrode and the two bottom channel electrodes. The environment was further regulated by flowing 5N ultra high-purity Ar at a controlled rate of 87 standard cubic centimeters per minute using an Omega mass flow controller. A Swagelok check valve maintained the chamber pressure at ≈50 torr above ambient pressure, further preventing air backflow. Monitoring with a Zirox ZR5 oxygen sensor indicates that the oxygen gas concentration in the chamber is about 3 ppm. The flowing Ar formed a more effective thermal contact between the heater and chip compared to testing the device in vacuum.

Retention, cyclic voltammetry, and switching measurements for 1 s or longer were conducted using a Bio-logic SP300 bipotentiostat with a common ground. For switching, we applied a ±2 V gate pulse for 1 s or longer; for retention, we applied 0 V on the gate. To measure the channel resistance, we applied a continuous 0.01 V across the channel. Switching measurements with a duration of less than 1 s were conducted using a National Instruments data acquisition device (DAQ-6358) system, as in previous work.[28] For switching, we applied a square wave between 2 and 8 V for between 0.8 and 50 ms. The read pulses consisted of 0.1 V pulses applied for 0.1 s after the write pulse. As shown in Figure S8, the current-voltage response of the channel is largely linear, so the resistance does not depend on the applied voltage. The switching voltage and duration for each measurement are included in the figure. The read speed and endurance measurements (Figure S2) were taken using a Keithley 4200A semiconductor parameter analyzer with a pulse measure unit.

STEM measurements

STEM analyses were carried out using a Thermo Fisher Scientific Talos F200X G2, a 200 kV scanning transmission electron microscope operating in STEM mode. Acquisition of STEM images and EDS data employed Velox software. STEM specimens were prepared utilizing a Thermo Fisher Scientific Helios G4 Plasma focused ion beam with the final beam condition set at 12 keV and 10 pA for liftout polishing.

RESOURCE AVAILABILITY

Lead contact

Requests for further information and resources should be directed to and will be fulfilled by the lead contact, Yiyang Li (yiyangli@umich.edu).

Materials availability

This work did not generate new unique reagents or materials.

Data and code availability

The data that support the findings of this study are publicly available at the Materials Commons 2.0 repository at https://doi.org/10.13011/m3-pmdj-mz08. This paper does not report original code.

ACKNOWLEDGMENTS

The work at the University of Michigan was supported by the National Science Foundation under grants ECCS-2106225 and CCF-2235316 and by a Sandia University Partnership Network (SUPN) program. Part of the fabrication of the devices was conducted at the University of Michigan Lurie Nanofabrication Facility. The authors acknowledge the University of Michigan College of Engineering for financial support and the Michigan Center for Materials Characterization for use of the instruments and staff assistance. We thank Dr. Kai Sun for assistance with the TEM sample preparation and measurements. The work at Sandia National Laboratories was supported by the Laboratory Directed Research and Development (LDRD) program. Sandia National Laboratories is a multi-mission laboratory managed and operated by National Technology and Engineering Solutions of Sandia, LLC, a wholly owned subsidiary of Honeywell International Inc., for the US Department of Energy's National Nuclear Security Administration under contract DE-NA-0003525.

AUTHOR CONTRIBUTIONS

J.L., A.A.T., E.J.F., and Y.L. conceived the idea. J.L. designed the experiments. J.L., A.J.J., S.Y.L., L.S.S., N.J.G., V.J.W., and L.A.C. fabricated ECRAM devices and performed device measurements. J.L. conducted transmission electron microscopy experiments. Y.L. supervised the project. All authors contributed to writing or revising the manuscript.

DECLARATION OF INTERESTS

The authors have filed a patent based on this work with the US Patent and Trademark Office.

SUPPLEMENTAL INFORMATION

Supplemental information can be found online at https://doi.org/10.1016/j.device.2024.100623.

Received: August 22, 2024
Revised: October 11, 2024
Accepted: November 6, 2024
Published: December 3, 2024

REFERENCES

1. Neudeck, P.G., Okojie, R.S., and Chen, L.-Y. (2002). High-temperature electronics - a role for wide bandgap semiconductors? Proc. IEEE *90*, 1065–1076. https://doi.org/10.1109/JPROC.2002.1021571.
2. Cressler, J.D., and Mantooth, H.A. (2017). Extreme Environment Electronics (CRC Press).
3. Neudeck, P.G., Spry, D.J., Chen, L., Prokop, N.F., and Krasowski, M.J. (2017). Demonstration of 4H-SiC Digital Integrated Circuits Above 800 °C. IEEE Electron. Device Lett. *38*, 1082–1085. https://doi.org/10.1109/LED.2017.2719280.
4. Kaneko, M., Nakajima, M., Jin, Q., and Kimoto, T. (2022). SiC Complementary Junction Field-Effect Transistor Logic Gate Operation at 623 K. IEEE Electron. Device Lett. *43*, 997–1000. https://doi.org/10.1109/LED.2022.3179129.
5. Yuan, M., Xie, Q., Niroula, J., Isamotu, M.F., Rajput, N.S., Chowdhury, N., and Palacios, T. (2022). High Temperature Robustness of Enhancement-Mode p-GaN-Gated AlGaN/GaN HEMT Technology. In 2022 IEEE 9th Workshop on Wide Bandgap Power Devices & Applications (WiPDA), pp. 40–44. https://doi.org/10.1109/WiPDA56483.2022.9955304.

6. Jo, E., Kang, Y., Sim, S., Lee, H., and Kim, J. (2023). High-Temperature-Operable Electromechanical Computing Units Enabled by Aligned Carbon Nanotube Arrays. ACS Nano *17*, 13310–13318. https://doi.org/10.1021/acsnano.3c01304.

7. Suga, H. (2024). High-temperature non-volatile memory technology. Nat. Electron. *7*, 330–331. https://doi.org/10.1038/s41928-024-01172-6.

8. Pradhan, D.K., Moore, D.C., Francis, A.M., Kupernik, J., Kennedy, W.J., Glavin, N.R., Olsson, R.H., and Jariwala, D. (2024). Materials for high-temperature digital electronics. Nat. Rev. Mater. *9*, 790–807. https://doi.org/10.1038/s41578-024-00731-9.

9. Suga, H., Suzuki, H., Shinomura, Y., Kashiwabara, S., Tsukagoshi, K., Shimizu, T., and Naitoh, Y. (2016). Highly stable, extremely high-temperature, nonvolatile memory based on resistance switching in polycrystalline Pt nanogaps. Sci. Rep. *6*, 34961. https://doi.org/10.1038/srep34961.

10. Drury, D., Yazawa, K., Zakutayev, A., Hanrahan, B., and Brennecka, G. (2022). High-Temperature Ferroelectric Behavior of $Al_{0.7}Sc_{0.3}N$. Micromachines *13*, 887. https://doi.org/10.3390/mi13060887.

11. Pradhan, D.K., Moore, D.C., Kim, G., He, Y., Musavigharavi, P., Kim, K.-H., Sharma, N., Han, Z., Du, X., Puli, V.S., et al. (2024). A scalable ferroelectric non-volatile memory operating at 600 °C. Nat. Electron. *7*, 348–355. https://doi.org/10.1038/s41928-024-01148-6.

12. Huang, M., Schwacke, M., Onen, M., del Alamo, J., Li, J., and Yildiz, B. (2023). Electrochemical Ionic Synapses: Progress and Perspectives. Adv. Mater. *35*, 2205169. https://doi.org/10.1002/adma.202205169.

13. Talin, A.A., Li, Y., Robinson, D.A., Fuller, E.J., and Kumar, S. (2023). ECRAM Materials, Devices, Circuits and Architectures: A Perspective. Adv. Mater. *35*, 2204771. https://doi.org/10.1002/adma202204771.

14. Fuller, E.J., Li, Y., Bennet, C., Keene, S.T., Melianas, A., Agarwal, S., Marinella, M.J., Salleo, A., and Talin, A.A. (2019). Redox transistors for neuromorphic computing. IBM J. Res. Dev. *63*, 1–9. https://doi.org/10.1147/JRD.2019.2942285.

15. Kwak, H., Kim, N., Jeon, S., Kim, S., and Woo, J. (2024). Electrochemical random-access memory: recent advances in materials, devices, and systems towards neuromorphic computing. Nano Converg. *11*, 9. https://doi.org/10.1186/s40580-024-00415-8.

16. Nikam, R.D., Lee, J., Lee, K., and Hwang, H. (2023). Exploring the Cutting-Edge Frontiers of Electrochemical Random Access Memories (ECRAMs) for Neuromorphic Computing: Revolutionary Advances in Material-to-Device Engineering. Small *19*, 2302593. https://doi.org/10.1002/smll.202302593.

17. Fuller, E.J., Gabaly, F.E., Léonard, F., Agarwal, S., Plimpton, S.J., Jacobs-Gedrim, R.B., James, C.D., Marinella, M.J., and Talin, A.A. (2017). Li-Ion Synaptic Transistor for Low Power Analog Computing. Adv. Mater. *29*, 1604310. https://doi.org/10.1002/adma.201604310.

18. Nguyen, N.-A., Schneegans, O., Salot, R., Lamy, Y., Giapintzakis, J., Mai, V.H., and Oukassi, S. (2022). An Ultralow Power Li_xTiO_2-Based Synaptic Transistor for Scalable Neuromorphic Computing. Adv. Electron. Mater. *8*, 2200607. https://doi.org/10.1002/aelm.202200607.

19. Li, Y., Fuller, E.J., Asapu, S., Agarwal, S., Kurita, T., Yang, J.J., and Talin, A.A. (2019). Low-Voltage, CMOS-Free Synaptic Memory Based on Li_xTiO_2 Redox Transistors. ACS Appl. Mater. Interfaces *11*, 38982–38992. https://doi.org/10.1021/acsami.9b14338.

20. Wan, Q., Rasetto, M., Sharbati, M.T., Erickson, J.R., Velagala, S.R., Reilly, M.T., Li, Y., Benosman, R., and Xiong, F. (2021). Low-Voltage Electrochemical Li_xWO_3 Synapses with Temporal Dynamics for Spiking Neural Networks. Adv. Intell. Syst. *3*, 2100021. https://doi.org/10.1002/aisy.202100021.

21. Tang, J., Bishop, D., Kim, S., Copel, M., Gokmen, T., Todorov, T., Shin, S., Lee, K.-T., Solomon, P., Chan, K., et al. (2018). ECRAM as Scalable Synaptic Cell for High-Speed, Low-Power Neuromorphic Computing. In 2018 IEEE International Electron Devices Meeting (IEDM), pp. 13.1.1–13.1.4. https://doi.org/10.1109/IEDM.2018.8614551.

22. van de Burgt, Y., Lubberman, E., Fuller, E.J., Keene, S.T., Faria, G.C., Agarwal, S., Marinella, M.J., Alec Talin, A., and Salleo, A. (2017). A non-volatile organic electrochemical device as a low-voltage artificial synapse for neuromorphic computing. Nat. Mater. *16*, 414–418. https://doi.org/10.1038/nmat4856.

23. Fuller, E.J., Keene, S.T., Melianas, A., Wang, Z., Agarwal, S., Li, Y., Tuchman, Y., James, C.D., Marinella, M.J., Yang, J.J., et al. (2019). Parallel programming of an ionic floating-gate memory array for scalable neuromorphic computing. Science *364*, 570–574. https://doi.org/10.1126/science.aaw5581.

24. Onen, M., Emond, N., Wang, B., Zhang, D., Ross, F.M., Li, J., Yildiz, B., and del Alamo, J.A. (2022). Nanosecond protonic programmable resistors for analog deep learning. Science *377*, 539–543. https://doi.org/10.1126/science.abp8064.

25. Yao, X., Klyukin, K., Lu, W., Onen, M., Ryu, S., Kim, D., Emond, N., Waluyo, I., Hunt, A., del Alamo, J.A., et al. (2020). Protonic solid-state electrochemical synapse for physical neural networks. Nat. Commun. *11*, 3134. https://doi.org/10.1038/s41467-020-16866-6.

26. Cui, J., An, F., Qian, J., Wu, Y., Sloan, L.L., Pidaparthy, S., Zuo, J.-M., and Cao, Q. (2023). CMOS-compatible electrochemical synaptic transistor arrays for deep learning accelerators. Nat. Electron. *6*, 292–300. https://doi.org/10.1038/s41928-023-00939-7.

27. Kim, S., Todorov, T., Onen, M., Gokmen, T., Bishop, D., Solomon, P., Lee, K.-T., Copel, M., Farmer, D.B., Ott, J.A., et al. (2019). Metal-oxide based, CMOS-compatible ECRAM for Deep Learning Accelerator. In 2019 IEEE International Electron Devices Meeting (IEDM), pp. 35.7.1–35.7.4. https://doi.org/10.1109/IEDM19573.2019.8993463.

28. Li, Y., Fuller, E.J., Sugar, J.D., Yoo, S., Ashby, D.S., Bennett, C.H., Horton, R.D., Bartsch, M.S., Marinella, M.J., Lu, W.D., and Talin, A.A. (2020). Filament-Free Bulk Resistive Memory Enables Deterministic Analogue Switching. Adv. Mater. *32*, 2003984. https://doi.org/10.1002/adma.202003984.

29. Noh, K., Kwak, H., Son, J., Kim, S., Um, M., Kang, M., Kim, D., Ji, W., Lee, J., Jo, H., et al. (2024). Retention-aware zero-shifting technique for Tiki-Taka algorithm-based analog deep learning accelerator. Sci. Adv. *10*, eadl3350. https://doi.org/10.1126/sciadv.adl3350.

30. Langner, P., Chiabrera, F., Alayo, N., Nizet, P., Morrone, L., Bozal-Ginesta, C., Morata, A., and Tarancòn, A. (2024). Solid-State Oxide-Ion Synaptic Transistor for Neuromorphic Computing. Preprint at arXiv. https://doi.org/10.48550/arXiv.2408.01469.

31. Freidzon, D., Wachtel, E., Cohen, H., Houben, L., Kossoy, A., Brontvein, O., Varenik, M., Frenkel, A.I., Ehre, D., and Lubomirsky, I. (2024). A Gd-doped ceria/TiOx nanocomposite as the active layer in a three terminal electrochemical resistivity switch. Solid State Ionics *411*, 116572. https://doi.org/10.1016/j.ssi.2024.116572.

32. Marinella, M.J., Bennett, C.H., Zutter, B., Siath, M., Spear, M., Vizkelethy, G., Xiao, T.P., Fuller, E., Hughart, D., Agarwal, S., et al. (2024). Heavy-Ion-Induced Displacement Damage Effects on WO_x ECRAM. IEEE Trans. Nucl. Sci. *71*, 579–584. https://doi.org/10.1109/TNS.2024.3360409.

33. Fang, R., Li, X., Ren, K., Zhang, W., Xu, H., Wang, L., and Shang, D. (2024). Improved dynamic characteristics of oxide electrolyte-gated transistor for time-delayed reservoir computing. Appl. Phys. Lett. *124*. https://doi.org/10.1063/5.0185402.

34. Chen, P., Liu, F., Lin, P., Li, P., Xiao, Y., Zhang, B., and Pan, G. (2023). Open-loop analog programmable electrochemical memory array. Nat. Commun. *14*, 6184. https://doi.org/10.1038/s41467-023-41958-4.

35. Lee, J., Nikam, R.D., Kwak, M., and Hwang, H. (2022). Strategies to Improve the Synaptic Characteristics of Oxygen-Based Electrochemical Random-Access Memory Based on Material Parameters Optimization. ACS Appl. Mater. Interfaces *14*, 13450–13457. https://doi.org/10.1021/acsami.1c21045.

36. Nikam, R.D., Kwak, M., and Hwang, H. (2021). All-Solid-State Oxygen Ion Electrochemical Random-Access Memory for Neuromorphic Computing. Adv. Electron. Mater. *7*, 2100142. https://doi.org/10.1002/aelm.202100142.

37. Porzani, M., Ricci, S., Farronato, M., and Ielmini, D. (2024). Programming Characteristics of Electrochemical Random Access Memory (ECRAM)—Part I: Experimental Study. IEEE Trans. Electron. Dev. *71*, 3240–3245. https://doi.org/10.1109/TED.2024.3376309.

38. Kang, H., and Woo, J. (2021). Cu-ion-actuated three-terminal neuromorphic synaptic devices based on binary metal-oxide electrolyte and channel. Appl. Phys. Lett. *119*, 072103. https://doi.org/10.1063/5.0059697.

39. Schwacke, M., Žguns, P., Del Alamo, J., Li, J., and Yildiz, B. (2024). Electrochemical Ionic Synapses with Mg^{2+} as the Working Ion. Adv. Electron. Mater. *10*, 2300577. https://doi.org/10.1002/aelm.202300577.

40. Kim, D.S., Watkins, V.J., Cline, L.A., Li, J., Sun, K., Sugar, J.D., Fuller, E.J., Talin, A.A., and Li, Y. (2023). Nonvolatile Electrochemical Random-Access Memory under Short Circuit. Adv. Electron. Mater. *9*, 2200958. https://doi.org/10.1002/aelm.202200958.

41. Skowronski, M. (2023). Material instabilities in the TaOx-based resistive switching devices (Invited). In 2023 IEEE International Reliability Physics Symposium (IRPS), pp. 1–5. https://doi.org/10.1109/IRPS48203.2023.10117796.

42. Li, J., Appachar, A., Peczonczyk, S.L., Harrison, E.T., Ievlev, A.V., Hood, R., Shin, D., Yoo, S., Roest, B., Sun, K., et al. (2024). Thermodynamic origin of nonvolatility in resistive memory. Matter *7*, 3970–3993. https://doi.org/10.1016/j.matt.2024.07.018.

43. Choi, S., Lee, J., Kim, S., and Lu, W.D. (2014). Retention failure analysis of metal-oxide based resistive memory. Appl. Phys. Lett. *105*, 113510. https://doi.org/10.1063/1.4896154.

44. Lee, M.-J., Lee, C.B., Lee, D., Lee, S.R., Chang, M., Hur, J.H., Kim, Y.-B., Kim, C.-J., Seo, D.H., Seo, S., et al. (2011). A fast, high-endurance and scalable non-volatile memory device made from asymmetric Ta2O5−x/TaO2−x bilayer structures. Nat. Mater. *10*, 625–630. https://doi.org/10.1038/nmat3070.

45. Kwak, H., Lee, C., Lee, C., Noh, K., and Kim, S. (2021). Experimental measurement of ungated channel region conductance in a multi-terminal, metal oxide-based ECRAM. Semicond. Sci. Technol. *36*, 114002. https://doi.org/10.1088/1361-6641/ac25c8.

46. Lee, J., Nikam, R.D., Kwak, M., and Hwang, H. (2022). Improved Synaptic Characteristics of Oxide-Based Electrochemical Random Access Memory at Elevated Temperatures Using Integrated Micro-Heater. IEEE Trans. Electron. Dev. *69*, 2218–2221. https://doi.org/10.1109/TED.2022.3151306.

47. Nikam, R.D., Lee, J., Choi, W., Kim, D., and Hwang, H. (2022). On-Chip Integrated Atomically Thin 2D Material Heater as a Training Accelerator for an Electrochemical Random-Access Memory Synapse for Neuromorphic Computing Application. ACS Nano *16*, 12214–12225. https://doi.org/10.1021/acsnano.2c02913.

48. Melianas, A., Quill, T.J., LeCroy, G., Tuchman, Y., Loo, H.v., Keene, S.T., Giovannitti, A., Lee, H.R., Maria, I.P., McCulloch, I., and Salleo, A. (2020). Temperature-resilient solid-state organic artificial synapses for neuromorphic computing. Sci. Adv. *6*, eabb2958. https://doi.org/10.1126/sciadv.abb2958.

49. Gonzalez-Rosillo, J.C., Balaish, M., Hood, Z.D., Nadkarni, N., Fraggedakis, D., Kim, K.J., Mullin, K.M., Pfenninger, R., Bazant, M.Z., and Rupp, J.L.M. (2020). Lithium-Battery Anode Gains Additional Functionality for Neuromorphic Computing through Metal–Insulator Phase Separation. Adv. Mater. *32*, 1907465. https://doi.org/10.1002/adma.201907465.

50. Tian, H., and Bazant, M.Z. (2022). Interfacial Resistive Switching by Multiphase Polarization in Ion-Intercalation Nanofilms. Nano Lett. *22*, 5866–5873. https://doi.org/10.1021/acs.nanolett.2c01765.

51. Min, K.-H., Sinclair *, R., Park, I.-S., Kim, S.-T., and Chung, U.-I. (2005). Crystallization behaviour of ALD-Ta_2O_5 thin films: the application of in-situ TEM. Philos. Mag. A *85*, 2049–2063. https://doi.org/10.1080/14786430500036546.

52. Garg, S.P., Krishnamurthy, N., Awasthi, A., and Venkatraman, M. (1996). The O-Ta (Oxygen-Tantalum) system. J. Phase Equil. *17*, 63–77. https://doi.org/10.1007/BF02648373.